Aerosol Optical Properties and its Radiative Effects in Northern China

Zhanqing Li[1], Xiangao Xia[2], Maureen Cribb[1], Wen Mi[1], Brent Holben[3], Pucai Wang[2], Hongbin Chen[2], Si-Chee Tsay[3], T. F. Eck[3], Fengsheng Zhao[1,4], E.G. Dutton[5], R.E. Dickerson[1]

1. Department of Atmospheric and Oceanic Science and ESSIC
University of Maryland
College Park, MD 20742

2. Institute of Atmospheric Physics
Chinese Academy of Sciences
Beijing, China

3. NASA Goddard Space Flight Center
Greenbelt, MD

4. National Satellite Meteorological Center
China Meteorological Administration, Beijing, China

5. NOAA/OAR/CMDL
GMD-1 325 Broadway, Boulder, CO 80305

Submitted to

Journal of Geophysical Research – Atmosphere

A special issue on

East-Asian Study of Tropospheric Aerosols: an International Regional Experiment

(EAST-AIRE)

Submitted: April 7, 2006

Revised: September 6, 2006

Abstract

As a fast developing country covering a large territory, China is experiencing rapid environmental changes. High concentrations of aerosols with diverse properties are emitted in the region, providing a unique opportunity for understanding the impact of environmental changes on climate. Until very recently, few observational studies were conducted in the source regions. The East Asian Study of Tropospheric Aerosols: an International Regional Experiment (EAST-AIRE) attempts to characterize the physical, optical and chemical properties of the aerosols and their effects on climate over China. This study presents some preliminary results using continuous high-quality measurements of aerosol, cloud and radiative quantities made at the first EAST-AIRE baseline station at Xianghe, about 70 km east of Beijing over a period of one year (September 2004 to September 2005). It was found that the region is often covered by a thick layer of haze (with a yearly mean aerosol optical depth equal to 0.82 at 500 nm and maximum greater than 4) due primarily to anthropogenic emissions. An abrupt "cleanup" of the haze often took place in a matter of one day or less due to the passage of cold fronts. The mean single scattering albedo is approximately 0.9 but has strong day-to-day variations with maximum monthly averages occurring during the summer. Large aerosol loading and strong absorption lead to a very large aerosol radiative effect at the surface (the annual 24-hour mean values equals 24 Wm^{-2}), but a much smaller aerosol radiative effect at the top of the atmosphere (one tenth of the surface value). The boundary atmosphere is thus heated dramatically during the daytime, which may affect atmospheric stability and cloud formation. In comparison, the cloud radiative effect at the surface is only moderately higher (-41 Wm^{-2}) than the aerosol radiative effect at the surface.

1. Introduction

Aerosols are a major factor influencing the Earth's radiation budget and may also affect the hydrologic cycle. By scattering and absorbing solar radiative energy, aerosols alter the radiation budgets at the top, bottom and interior of the atmospheric column [*Charlson et al., 1992*], which in turn affects the atmospheric heating rate and stability,further influencing cloud development and microphysics, as well as precipitation [*Hansen et al., 1997; Rosenfeld and Lensky, 1998; Kaufman et al., 2001; Ramanathan et al., 2001*]. Such impacts of aerosols on the radiation budget are usually referred to as the direct aerosol radiative effect (ARE) and semi-direct effect , although aerosol forcing is a term often used particularly for anthropogenic aerosols. Despite a substantial increase in our efforts to further understand aerosols and their climatic effects, aerosol radiative effects remain one of the largest uncertainties in climate studies [*IPCC 2001*].

To increase understanding of these issues, many recent investigations were committed to improving the global estimation of ARE. At the top of the atmosphere (TOA), estimates of global mean ARE obtained following different methods appear to converge to a value in the neighborhood of -5 Wm^{-2} [*Bellouin et al., 2005; Loeb and Manalo-Smith, 2005; Remer and Kaufman, 2005; Chou et al. 2002*]. It is worth noting, however, that these estimates were based on satellite retrievals of aerosol optical depth (AOD) from various sensors such as MODIS, TOMS, POLDER, and CERES. It is widely known that satellite AOD retrievals are mainly valid over dark targets such as oceans and vegetated land surfaces, but a few satellite sensors (e.g., MISR, POLDER) are valid over bright land and snow/ice surfaces. In light of the common shortcomings suffered by various satellite retrievals, the narrow range of ARE estimates does not

81 necessarily lend enough confidence on the ARE. Also, satellite retrievals of ARE are limited to
82 clear-sky conditions, while the all-sky ARE is also important but more difficult to derive [*Li and*
83 *Trishchenko, 2001*].

84 Estimation of the ARE at the surface is as important as that at the TOA. Due to variable
85 aerosol absorption, the surface ARE is larger and more variable than the ARE at the TOA [*Li,*
86 *1998; Li and Kou, 1998; Satheesh and Ramanathan, 2000*]. It is much more challenging to
87 estimate the ARE at the surface because it requires good knowledge of three aerosol variables,
88 namely, the spectral AOD, the aerosol single scattering albedo (SSA) and the asymmetry factor.
89 The latter two are extremely difficult to derive from conventional satellite observations [*King et*
90 *al. 1999; Kaufman et al., 2001, 2002*]. To date, most global estimates of ARE at the surface
91 have been made by model simulations of different aerosol species [*Takemura et al., 2005; Liao*
92 *et al, 2004; Kim and Ramanathan, 2006*]. Due to inherent model assumptions and error
93 propagation, estimates of surface AREs are prone to considerable uncertainties.

94 Both satellite-based and model-based estimates of ARE require validation using in-situ
95 and ground-based observations. As a result of high spatial and temporal variations in aerosol
96 loading and optical properties, extensive observations need to be carried out in all major aerosol
97 source regions. Ground observation is the most reliable means of estimating the ARE at the
98 surface. Unfortunately, the existing ground-based observation networks such as the Aerosol
99 Robotic Network (AERONET) [*Holben et al., 1998*] and the Baseline Surface Radiation
100 Network (BSRN) [*Ohmura et al., 1998*] reside chiefly in developed regions where aerosol
101 loading is generally lower than in developing regions. Fewer high-quality and long-term ground
102 observation stations are located in major aerosol source regions such as the Africa, Asia, and
103 South America. At present, the total number of AERONET sites are 36 in North America, 24 in

Europe, but only 18 in Asia, 10 in Africa, 11 in South America, and 16 over all oceanic sites . By contrast, the average AOD observed in the latter two regions are more than twice the value in the former two regions.

As a fast developing and densely populated region in the world, Asia is a major source of aerosols whose loadings are high and chemical/physical properties are complex [*Li, 2004*]. To date, a handful of field experiments have been conducted in Asia such as the Indian Ocean Experiment (INDOEX) [*Ramanathan et al., 2001*], the Asian-Pacific Regional Aerosol Characterization Experiment (ACE-Asia) [*Huebert et al., 2003*], and the Asian Atmospheric Particle Environment (APEX) [*Nakajima et al., 2003*]. Many important findings were made from these experiments such as the generally strong absorption of Asian aerosols [*Satheesh and Ramanathan, 2000; Kim et al., 2004*], the modification of dust aerosols by air pollutants *[Kim et al.*, 2005], etc. Despite the significant accomplishments achieved by these experiments, a fundamental limitation still exists, namely, that few in-situ observations were made in the continental source regions on a continual basis. Except for the short-term operation of some basic measurements made at a few sites in China, substantially more observations must be made in order to portray the spatial and temporal variations of the complex aerosols in the vast territory of China.

To fulfill this goal, the East Asian Study of Tropospheric Aerosols: an International Regional Experiment (EAST-AIRE) has been conducted by American and Chinese scientists since 2004. A primary goal of the study is to acquire aerosol optical, physical and chemical properties and understand their climatic effect through means of ground-based, air-borne and space-based observations. The observational component of the study consists of extensive measurements of aerosol, cloud and radiation quantities at 5-6 baseline stations, spectral aerosol

127 loading measurements made at 25 stations as part of China's Ecological Research Network [*Xin*
128 *et al., 2006*], and short-term intensive observation campaigns measuring aerosol chemical and
129 physical properties as well as precursor gases on the ground and in the air [*Li et al., 200;*
130 *Dickerson et al., 2006; Huebert et al., 2006*].

131 This study makes use of measurements made since September 2004 at the first EAST-
132 AIRE baseline station in Xianghe, China. The observation quantities used in the study are
133 described in section 2. The data are classified as clear-clean, clear-hazy, and cloudy for
134 determining aerosol and cloud radiative effects. The methods of scene identification are
135 introduced in section 3. The aerosol optical properties are discussed in Section 4. Section 5
136 presents the results of aerosol and cloud radiative effects. Conclusions from the study are given
137 in Section 6.

138

139 **2. Radiation, aerosol and cloud data sets**

140

141 This study employs data collected at Xianghe (39.753^{o}N, 116.961^{o}E), the first EAST-
142 AIRE observatory. The area is mostly plain-like with little variation in elevation. Surrounded by
143 agricultural land, densely populated residences and light industries. Sitting between two mega-
144 cities (with Beijing 70km to the northwest and 70km Tianjin to the southeast) and less than 5 km
145 west of the local town center (with a population of ~50,000), the site experiences both natural
146 aerosols and anthropogenic pollutants of urban, rural, or mixed origins pending on the wind
147 direction. It began operation on September 21, 2004 and since then, has been taking continuous
148 measurements of various radiative and aerosol quantities, as well as collecting animations of the
149 sky conditions. The data are displayed on a near real-time basis at

150 http://www.atmos.umd.edu/~yuan/web_proj/Xianghe/FrameSet_test.htm. This allows us to
151 perform data quality checks and promptly fix any problem that may arise. Table 1 lists all the
152 instruments installed at the Xianghe site.

153 For radiation observations, the site is equipped with both independent and redundant
154 instruments for quality control purposes. Total downwelling shortwave (SW; 0.3-3 μm) radiation
155 is measured with Kipp and Zonnen's CM21 and CM11 radiometers. Diffuse SW radiation is
156 measured with a black and white pyranometer (8-48) with a shadowing disc and direct SW
157 radiation is measured with a normal incidence pyrheliometer (NIP), both manufactured by
158 Eppley. All radiation measurements are taken at a 1-minute temporal resolution. The NIP was
159 mounted on an EKO STR-22 solar tracker pointing towards the sun, while the 8-48 was placed
160 on the base of the tracker so that the direct solar beam is constantly blocked by a solar disk. In
161 addition to program-controlled movement, the tracker has a photo-sensitive detector to adjust the
162 position for precise pointing. Since its installation, the solar tracker has worked very stably and
163 precisely. No routine manual adjustment has been necessary so far. Total downwelling SW
164 radiation was thus measured with four instruments which provide independent measurements for
165 inter-comparison and validation purposes. It turns out to be a very effective means of quality
166 control. During the period of operation, we identified a few problems that were promptly fixed.
167 Overall, observations from the different instruments agree with each other within 10 Wm^{-2}, often
168 less than 5 Wm^{-2}. Larger disagreements occurred occasionally due to differences in the response
169 time for fast moving clouds, or the misalignment of the solar tracker. The problems were
170 identified and fixed and the data were corrected using good-quality data thanks to the redundant
171 measurements. In addition to the continual cross-comparison of data from different instruments,
172 instrument degradation was also monitored via annual comparisons against new or newly

calibrated radiometers that were brought to China for establishing new observation sites. So far, the instruments have performed very well with no noticeable degradation after 1.5 years of operation. The discrepancies are well within the specified instrument uncertainties.

In addition, several other radiation instruments are in operation including Epply's Precision Infrared Radiometer for measuring infrared radiation, Kipp and Zonnen's PAR-LITE quantum sensor for measuring photosynthetically active radiation (PAR; 0.4-0.7 μm), Eppley's total ultraviolet radiometer for measuring ultraviolet radiation, and a multi-filter rotating shadowband radiometer manufactured by Yankee Environmental Systems Inc. for measuring spectral shadowed and unshadowed irradiances. The data quality and continuity have complied with the high standards of the BSRN [*Ohmura et al. 1998*]. As a result, the station has been admitted to the BSRN network, the first such site in China. The data are available from the BSRN central archive, while quick data browsing can be seen from the EAST-AIRE web site: http://www.atmos.umd.edu/~yuan/web_proj/station.htm.

Also deployed at the site is a Cimel-318 sunphotometer, as a part of the AERONET [*Holben et al., 1998*]. The Cimel sunphotometer is a multi-channel, automatic sun-and-sky scanning radiometer that measures the direct solar irradiance and sky radiance at the Earth's surface. Measurements are taken at discrete wavelengths (340, 378, 440, 499, 613, 870, 940 and 1020 nm) to determine atmospheric transmissions of direct solar radiation and sky radiances. The direct and diffuse radiances are used to derive aerosol optical depth, size distribution and single scattering albedo [*Dubovik et al., 2002*]. Primarily uncertainties in calibration result in a total uncertainty of ~0.010-0.021 in computed aerosol optical depth for AERONET field instruments (which is spectrally dependent with the higher errors in the UV; Eck et al. [1999]) Retrieval of the aerosol single scattering albedo can be achieved for high aerosol optical depths (>0.4 at 0.440

196 μm) and for large solar zenith angles (>50^0) with an accuracy of ~0.03. The instrument is
197 weather-proof and requires little maintenance even during periods of adverse weather conditions.
198 Two levels of AERONET products are used in this study: level 2.0 data (cloud-screened and
199 quality-assured) and level 1.5 data (cloud-screened) when level 2.0 data were unavailable. As of
200 this writing, level 2.0 data are available from September 2004 to June 2005; level 1.5 data are
201 used for dates after June 2005.

202 A primary issue regarding the uncertainty of the AERONET AOD is cloud screening. A
203 strict cloud-screening algorithm was applied by examining the temporal variability of measured
204 AOD [*Smirnov et al., 2000*] for a set of three measurements (a triplet) made 30 seconds apart. In
205 order to discriminate clouds, the variability of the triplet AOD is examined first and when the
206 variability is either smaller than 0.02 or 0.03*AOD (whichever is higher), the data are accepted
207 for the next test. All data that fail this triplet stability test are classified as cloudy. If the test is
208 passed, a diurnal stability test is applied and if the standard deviation of the AOD at 500 nm is
209 less than 0.015, the measurement is classified as cloud-free. If the data fails this test, smoothness
210 of the data temporal variability is checked by limiting the second derivative of the AOD with
211 respect to time within certain values. This test helps remove thin cirrus clouds. AOD at 500 nm
212 and the Angstrom exponent are required to fall within three standard deviations for each day.
213 While the method effectively eliminates most cloud-contaminated data, it may discard data
214 associated with variable aerosols such as smoke plumes. Also, it may fail to detect very thin
215 stable cirrus clouds [*Kaufman et al., 2005*]. This may not pose a serious problem for this study
216 because the aerosol loading at Xianghe is generally heavy.

217 To help separate cloudy and hazy conditions, a total sky imager (TSI-440) was set up at
218 the site, which takes snapshots of the sky on a continuous 1-minute basis during each day from

sunrise to sunset. The TSI-440 model is a full color sky camera with a software package that operates the instrument and performs some data processing functions. It was designed for long-term field operation. It captures images in JPEG format data files, which can be analyzed for fractional cloud cover. From the high-frequency snapshot images, a movie of the sky conditions is generated for each day. It has proven to be a very useful tool to assist in the separation of cloudy scenes from hazy clear-sky scenes, as clouds are generally more variable than the atmospheric aerosols, including thin cirrus clouds. Like the other instruments, very little maintenance is required other than daily cleaning of the mirror.

All ground-based instruments have been operating without any interruption since the commencement of operation in September 2004. From February to June 2005, more instruments were brought to China for field campaign studies. A micro-pulse lidar (MPL) was deployed at the Xianghe site as a part of NASA's MPL network (http://mplnet.gsfc.nasa.gov) and provided information regarding the vertical profiles of aerosol and clouds. These data were useful for separating clouds from aerosols, due to certain unique features in the vertical layering. Clouds usually exhibit distinct boundaries with sharp attenuation above the ground, whereas aerosols show a gradual variation and continue to the ground.

In addition to ground-based measurements, this study also employs satellite measurements of SW fluxes reflected at the TOA obtained from the Clouds and the Earth's Radiant Energy System (CERES). The CERES instrument, deployed on the Earth Observing System's Terra and Aqua satellite platforms, consists of a scanning radiometer collecting radiometric measurements in the shortwave (0.3 – 5 μm), longwave (8 – 12 μm) and broadband (0.3 – 100 μm) channels [*Wielicki et al.*, 1996]. Onboard calibration is performed, leading to an accuracy of 1% in the radiance measurements. A spectral correction algorithm is applied to the

242 filtered measurements, producing unfiltered radiances corrected for the spectral response. Once
243 the scene type is identified, the appropriate angular distribution model is applied to the unfiltered
244 radiances and instantaneous TOA flux estimates result. One set of products from the CERES
245 instruments is the Single Satellite Footprint (SSF) collection of hourly products. The SSF data
246 are an integration of the coarser resolution CERES measurements (about 20 km at nadir) and
247 data from higher-resolution imagers such as MODIS on the Terra and Aqua platforms. In
248 general, two measurements were available for each day, one in the morning from the Terra
249 platform and another in the early afternoon from the Aqua platform. As of this study, the data
250 from the two platforms were available from October 2004 to June 2005 for Terra and October
251 2004 to March 2005 for Aqua. From July to October 2005, no SSF data were available and so the
252 CERES-ES8 product on the Aqua and Terra platforms were used. The SSF data are more
253 accurate than the ES-8 product due to the use of a more advanced angular dependence model
254 [Loeb et al., 2005].
255 TOA reflected shortwave fluxes, solar zenith angles, and precipitable water amounts
256 from the two CERES products for pixels located within a 50x50 km^2 area centered on Xianghe
257 were averaged and used as input into the models of *Li et al.* [1993] and *Li and Garand*[1994] in
258 order to retrieve the surface net radiation and the surface albedo, respectively. Only those
259 measurements made under clean background conditions (AOD<0.2) were used for retrieving
260 surface albedo and for checking the compatibility between point-based ground observations and
261 spatial observations from satellite. Satellite-retrieved downwelling total surface shortwave fluxes
262 using the algorithm of *Li et al. [2003]* were averaged over an area of 50x50 km^2 and compared
263 to the single-point ground measurements made at Xianghe. The agreement is generally good with
264 a mean difference of 0.91 Wm^{-2} and a standard deviation of about 14 Wm^{-2}. This suggests that

265 the ground-based measurements represent well the spatial scale of the satellite data so that the
266 aerosol effect determined from the two data sources can be compared and combined to derive the
267 aerosol effect in the atmosphere.
268
269 **3. Scene Identification**
270
271 For studying the ARE, a major challenge is the separation of cloudy and clear scenes.
272 This may not be difficult in a relatively clean atmosphere, but it poses a serious challenge over
273 our study area. Aerosol loading is often very high, making it problematic to readily distinguish
274 between hazy and cloudy conditions. Various methods of discriminating clear-hazy and cloudy
275 scenes were attempted but none seem to work under all circumstances. So to achieve the best
276 discrimination between clear-hazy and cloudy scenes a combination of the application of
277 automatic algorithms and visual inspection of various datasets was done.
278 Two objective methods of determining clear-sky periods were explored. One technique
279 developed by *Long and Ackerman* [2000] consists of a series of tests based on the magnitude and
280 temporal variability of the diffuse and total surface SW radiation measurements. The method
281 involves four tests of increasing complexity. If all four tests are passed, the observations are
282 classified as being made under clear-sky conditions. Only observations made when the solar
283 zenith angle is less than 80^{o} are considered when applying these tests. The first test determines
284 whether the downwelling total surface SW fluxes, normalized by a power law function of the
285 cosine of the solar zenith angle (μ), falls within a range of values typical for clear skies. The
286 coefficients used for normalization are first derived from the best-fits of a power law function
287 applied to data measured on specific days that are manually identified as containing substantial

periods of clear-sky intervals. These coefficients are interpolated for testing data on intervening days. The coefficients determined by the best-fitting algorithm are used to calculate the normalizing factor and upper and lower limits to the clear-sky acceptable values. In general, this test using minimum and maximum limits specific to data from Xianghe, works well in determining if clear skies are present.

The second test determines whether the downwelling diffuse radiation reaching the surface falls below a predetermined maximum value of 120 Wm^{-2}. This value is based on visual inspection of years of data obtained over the Southern Great Plains in the United States. For clear days with low aerosol loading (AOD<0.2) as often seen in that region, this limit is an acceptable value. A problem arises when there is significantly more aerosol loading under a cloudless sky. In these instances, the diffuse SW radiation reaching the surface contains a contribution from the aerosol layer which increases as the aerosol load increases. This results in a maximum value for diffuse SW radiation greater than the suggested 120 Wm^{-2}. From visual inspection of the diffuse SW radiation reaching the surface on cloudless days under a wide range of aerosol loading at Xianghe, we set the upper limit at 200 Wm^{-2}.

The third test involves comparing the change in downwelling surface SW fluxes over a small time interval with the change in downwelling TOA radiation during the same time interval. If there are no obstructions in the way (i.e. cloud or significant aerosol layer), the absolute change in magnitude of the fluxes at the surface over a small time interval should be less than the absolute change at the TOA. Given the absolute changes in the fluxes at the TOA over short time periods (10 minutes was chosen), an envelop of minimum and maximum limits was calculated and the changes in downwelling surface shortwave fluxes over the time period were tested to see

310 if the values fall within this envelop. In general, periods of clear sky were identified correctly
311 with this test, using the measurements taken at Xianghe.

312 The final test examines the variability of the normalized diffuse ratio, which is the diffuse
313 downwelling shortwave flux divided by the total downwelling shortwave flux, normalized by a
314 power law function of μ. The diffuse ratio can pick up subtle changes in the variability of
315 radiation reaching the surface over time and this variability is tested by calculating the running
316 mean and standard deviation of data from the mean during 11-minute periods. The clear-sky
317 detection limit was chosen to range between 0.0010 and 0.0015, a subjective value based on the
318 analysis of all data in the study of *Long and Ackerman* [2000]. Application of this test to data
319 from Xianghe had mixed results. Even on clear days with low aerosol loading, some of the
320 groups of data failed the test, i.e. the standard deviations were greater than 0.0015 for some 11-
321 minute periods.

322 Although most of the tests used to eliminate cloudy periods performed well with data
323 from Xianghe, not all worked ideally. Days of high aerosol loading, a frequent occurrence at the
324 observation site, poses a challenge. A technique for distinguishing between clear and cloudy
325 scenes, proposed by *Conant et al.* [1997], was attempted. They applied a peak frequency
326 distribution method to high-resolution total downwelling surface SW fluxes taken over the
327 central equatorial Pacific. This method is based on the premise that for downwelling surface SW
328 radiation measurements taken at a fixed solar zenith angle (+/-0.5^{o}), atmospheric transmittances
329 under clear-sky conditions do not change very much. If the sky is cloudy, atmospheric
330 transmittances are more variable. The technique involves plotting histograms of the
331 transmittances measured during incremental solar zenith angle ranges and examining the
332 presence of one sharp peak (clear sky) or multiple peaks spread over a range of transmittances

(cloudy sky). This technique was applied to the downwelling surface SW radiation measurements made at Xianghe. Although the technique was developed using flux measurements made over the central equatorial Pacific where there is little aerosol in the atmosphere, it works reasonably well when applied to data at Xianghe taken under clear skies in the presence of a moderate aerosol load (AOD ~ 1). In general, this method is fairly simple to implement and serves as an objective complementary tool to identify clear skies.

To take advantage of all data available and to increase the confidence of clear-hazy and cloudy sky discrimination, the detection results were subject to visual inspection using data from the radiometers, TSI, and MPL. Under many circumstances, the sky condition can be visually grasped by the overall shape, magnitude and smoothness in the times series of the total, direct and diffuse fluxes. If the sky is clear, the curve is generally smooth, although a smooth curve may not always correspond to a clear sky. The curve can be smooth at times under uniform overcast skies. In this case, the magnitude of the fluxes aid in assessing the sky condition. If there is the passage of cloud, the curve tends to be jagged. Inspection of hundreds of TSI movies helped gain a good sense of whether clouds were present. Given the general uniformity of the haziness over time during a given day, the presence and passage of clouds is visually evident through noticeable changes in the density of the radiant energy captured by the TSI imagery. But it is inevitable to occasionally misidentify cloudy and hazy conditions. When the MPL images were available (from March to June 2005), they further helped confirm the sky condition. AERONET AOD retrievals at 500 nm also aided in further reclassifying the clear-sky periods as either clear-clean (AOD<0.2) or clear-hazy (AOD>0.2).

4. Aerosol Optical Properties

Figure 1 shows the daily mean AOD measured by the Cimel sunphotometer at the Xianghe site from September 2004 to September 2005. The most striking feature is that the AOD is very high on many days, while the lowest "background" value is not much different from other typical continental sites (ranging from 0.1-0.2). To place these numbers in context, the global mean 500 nm AOD derived from all AERONET sites weighted by areas over which the data may represent is 0.13. The seasonal variation seems a lot weaker than the day to day variation, but are still significant, with the largest value occurring in August 2005 (monthly mean 500 nm AOD=1.7) and the lowest in January 2005 (monthly mean AOD=0.39).

In addition to a potential seasonal change in emissions, hygroscopic growth due to the swelling effect is likely a major factor [*Eck et al.*, 2005; *Jeong et al.*, 2006] because the summer is much more humid. This is partially supported by the plot of the Angstrom exponent (AE; derived from AOD measurements made at 440 nm and 870 nm) as a function of AOD (Fig. 2). There appears to be a general negative relation, implying that high AODs tend to be associated with larger aerosol particles. Clear positive relations are also seen between AOD and the relative humidity (Fig. 3). This suggests that the swelling effect played a certain role in the aerosol episodes, however stronger airmass stagnation episodes in summer (when RH is high) may also contribute to this apparent correlation.. The large range of the AE, from less than 0.2 to close to 2.0, suggests that there were different types of aerosols present (from very fine mode pollution to large coarse mode dust). The change in aerosol particle size in the fine mode is also induced by coagulation which increases with increasing aerosol loading. *Eck et al.* [2005] discussed the mechanism of coagulation in detail with data collected from another Asian site in Korea.

Strong aerosol episodes are the most striking feature of AOD changes in the region. This is more visible in the upper panel of Figure 4 which is the same as Fig. 1 but for October 2004. The lower panel shows measurements of the direct solar radiation reaching the ground. A gradual increase in 500 nm AOD over a period of 10 days is seen, starting from a very clean environment with AOD~0.1 to a polluted environment with AOD values up to 3.5. Aerosol samples and precursor gases (SO2, NOy, CO, O_3, etc.) were collected and analyzed during an Intensive Observation Period (IOP) conducted at the Xianghe site. It was found that changes in the concentrations of SO_2, CO, OC were at par with the total aerosol loading, suggesting that the episodes are mostly anthropogenic [*Li et al., 2006; Huebert et al., 2006*]. While the buildup is slow, the cleanup seems much faster. For the two episodes shown here, the AOD plunged from a peak value to a "background" value over the course of one day. Analysis of weather data indicates that the episodes were driven by the frontal activities that were associated with changes in airmass [*Li et al., 2006*]. The cold fronts were often accompanied by abrupt changes in wind direction, temperature, and humidity. Wet scavenging does not seem to be a dominant mechanism.

It is worth noting that the surface solar radiation budget is considerably affected by changes in the AOD. Not only do the periods of the oscillation in the two quantities coincide well with each other, the magnitudes of the changes are also proportional. Due partially to the heavy aerosol loading, the total amount of diffuse radiation reaching the ground is more than the amount of direct radiation, as there was little cloud cover in the month.

Figure 5 shows the SSA retrieved from the Cimel sunphotometer at four wavelengths from September 2004 to September 2005. Given possible biases due to calibration and/or the assumed surface albedo, only those SSA corresponding to AOD at 440 nm greater than 0.4 are

401 shown in the figure. The mean values are 0.921, 0.922, 0.913 and 0.908 at 441, 673, 873, and
402 1022 nm, respectively. These values are low compared to those measured at the majority of
403 AERONET sites. They are slightly larger than those reported for Mexico City and the Maldives
404 [*Dubovik et al., 2002*]. There is a weak seasonal trend in the SSA, with large values occurring
405 during the summer and smaller values during late fall to early winter. Again, the day-to-day
406 variation is much more dominant throughout the year.

407 To gain a further insight into the changes, the SSA is plotted as a function of the 500 nm
408 AOD and AE (Fig. 6). The SSA tends to increase with the AOD, but decrease with the AE. This
409 may result from the mixed influence of the hygroscopic growth, coagulation growth and variable
410 species of aerosol emissions from various sources, such as coarse mode airborne soil desert dust
411 versus fine mode smoke and pollution. For a fixed aerosol composition, the fine mode growth
412 effect enhances scattering (thus increasing the AOD), weakens the aerosol absorption efficiency
413 (thus increasing the SSA), and enlarges the particle size (thus decreasing the AE). Therefore, this
414 effect can explain the general trends shown in both plots. The good correlation between the
415 AOD and SO_2 episodes [*Li et al., 2006*] also indicate that the highly scattering and hygroscopic
416 sulfate aerosol is a major component of the aerosol species. This is confirmed by the chemical
417 analyses of aerosol particles collected at the site during the IOP [*Huebert et al., 2006*] which
418 showed a much higher concentration of sulfate than calcium for each aerosol episode observed in
419 March 2005.

420

421 **5. Radiative Effects of Aerosols and Clouds**

422

423 The heavy loading and strong absorption of aerosols found in Xianghe can exert a
424 substantial influence on the direct aerosol radiative effect on the ground. When heavy and strong
425 absorbing aerosols are present, caution must be exercised not to mix the aerosol radiative effect
426 with the cloud radiative effect [*Li and Trishchenko*, 2001]. We attempted to first separate the
427 two effects by first classifying scene types into clear-clean, clear-hazy and cloudy conditions.
428 Following the aforementioned scene identification methodology, we obtained classification
429 results for every day and analyzed them on a monthly basis in order to determine the monthly
430 mean effect. Figure 7 shows the classification results for March 2005 which was when the IOP
431 was conducted and when daily manual reports of the sky condition were made. The top panel
432 shows clear-sky measurements of downwelling SW flux, the middle panel shows cloudy-sky
433 (both partly cloudy and overcast) measurements of downwelling SW flux, and the bottom panel
434 combines the downwelling SW flux for both clear and cloudy scenes. The clear data points form
435 rather smooth and straight lines, whereas the cloudy data are much more variable. Another
436 important feature seen in the upper panel is that the magnitude of the downwelling flux varies
437 considerably. For a fixed solar zenith angle, the difference between the highest (cleanest) and
438 lowest (haziest) fluxes can reach 200 Wm^{-2}. Such large instantaneous aerosol radiative effects
439 have rarely been observed before, except in the biomass burning season in southern Amazonia
440 (Schafer et al, 2002).
441 The large variability in the atmospheric aerosol loading creates difficulty in determining the
442 cloud radiative effect (CRF). In some previous studies, the CRF was determined by the
443 deviation of all data points from the highest values (except for a few scattered data points caused
444 by cloud side scattering) to serve as clear-sky background value. If this method was adopted
445 here, the CRF would be substantially overestimated because a considerable portion of the

apparent CRF is actually caused by aerosols [*Li and Trishchenko, 2001*]. To account for the influence of aerosols, all cloud-free data were employed to determine the mean clear-sky values as a reference for determining the CRF. In determining ARE, one may either use the highest curve as a clear-sky background, or use model-computed values. When the AOD is less than 0.2, the observed values agree very well with values computed by a radiative transfer model [*Nakajima and Tanak*a, 1988]; the mean difference between the two is 7.6 Wm^{-2}.

Following this procedure, monthly mean cloud and aerosol surface radiative effects were estimated using the 1-minute measurements of total downwelling fluxes. The first step is to generate scatterplots like Fig. 7 for each month. The cosines of the solar zenith angle , ranging from 0.1 to nearly 1 (depending on the month), were separated into eighteen bins. The averages of all clear and cloudy fluxes as well as the maximum values within all the bins were determined. Three differences were computed: (1) differences between the mean clear values and the maximum values for determining the ARE ($\Delta F_{bin\text{-}aer}$), (2) differences between the mean cloudy and clear data for estimating CRF ($\Delta F_{bin\text{-}cld}$), and (3) differences between the mean of all data and the maximum values for determining the total effect due to both clouds and aerosols $\Delta F_{bin\text{-}all}$.

The monthly mean values were determined by integrating the differences over local time from sunrise to sunset averaged over a month. The integration variable was then converted from local time to μ using the following trigonometric relation:

$$\mu = \sin\phi\sin\delta + \cos\phi\cos\delta\cos(ct), \qquad (1)$$

where ϕ is the latitude, δ is the declination, $c=\pi/2$ hr, and t is the local time in decimal hours. Differentiating with respect to t, the conversion function is given by

$$f(\mu) = \frac{dt}{d\mu} = -\frac{1}{c\sqrt{(\cos\phi\cos\delta)^2 - (\mu - \sin\phi\cos\delta)^2}} \quad . \qquad (2)$$

468 The monthly daily mean cloud or aerosol effect, F_a, then becomes

469 $$F_a = \frac{1}{T}\int_0^T \Delta F_{bin}(t)\cdot dt = \frac{1}{T}\int_{\mu_{0\_min}}^{\mu_{0\_max}} f(\mu)\cdot \Delta F_{bin}(\mu)\cdot d\mu, \quad (3)$$

470 where T =12 hours. $\Delta F_{bin}(\mu)$ represents either $\Delta F_{bin\text{-}cld}$, or $\Delta F_{bin\text{-}aer}$, or $\Delta F_{bin\text{-}all.}$ The limits of the
471 integration are the minimum and maximum values of μ for a particular month of data.

472 The monthly means of the radiative effect due to aerosol, cloud and their combination are
473 shown by the bar graphs in Figure 8. The magnitudes of the effects are large in general,
474 especially for the ARE. The annual mean values of the aerosol, cloud and total radiative effects
475 are -24.1, -41.0 and -53.9 Wm^{-2}, respectively. Note that the total effect is not equal to the sum of
476 the two components. As a reference, recent estimates of the global mean surface ARE range
477 from –7 Wm^{-2} to –10 Wm^{-2},derived from a combination of MODIS and GOCART [*Yu et al.,*
478 *2004*] and POLDER and AERONET [*Bellouin et al., 2003*] data. Chung et al. (2005) used
479 MODIS, AERONET and GOCART products to derive a global annual mean surface ARE equal
480 to -3.4 Wm^{-2} .

481 Monthly means of the ARE at the TOA were also calculated using the TOA SW fluxes
482 obtained from the CERES SSF products. The satellite data were matched with surface
483 measurements that were classified as associated with clear-clean, clear-hazy, or cloudy sky
484 conditions. Separate scatterplots were generated for TOA reflected fluxes and surface
485 downwelling SW fluxes as functions of μ (Fig. 9). In contrast to the clear separation between
486 clear and hazy data on the surface plot, there is a no clear distinction for the TOA data points.
487 This implies that the addition of heavy aerosols in the region does not increase reflection in the
488 atmosphere-surface system. Changes in TOA reflection are dictated by a combination of aerosol
489 parameters (SSA, AOD, backscattering fraction) and surface albedo. It is a combination of these

490 variables results in a near neutral aerosol effect. During the INDOEX, TOA ARE was
491 significantly smaller than at the surface but the TOA ARE in that region (the Indian Ocean) is
492 not as small as that found at the Xianghe site, even though the SSA values are less over the
493 Indian Ocean than at the Xianghe site. This is because the surface albedo of the Indian Ocean is
494 much darker than the land area surrounding Xianghe. We estimated the surface broadband
495 albedo from CERES TOA reflectances using the algorithm of *Li and Garand* (1994) for all clear-
496 clean days during the year. The surface albedo varied from 13% during the summer when the
497 area is dominated by crops to 20% during the winter when the land is bare soil. The higher
498 surface albedo (relative to the ocean surface albedo) increases the chances of absorption of
499 photons traveling upward, and also decreases the contrast between surface brightness and the
500 scattering effects of the aerosol layer.

501 The retrieval of the surface solar radiation budget from satellite data is difficult because
502 the retrieval algorithms [e.g., *Li et al., 1993; Zhang et al. 2005]* essentially rely on coupled
503 changes between reflected flux at the TOA and at the surface. For clouds, this is not a problem
504 due to the very high single scattering albedo. For absorbing aerosols, it poses a serious
505 problem, as demonstrated in Fig. 10 which shows the comparisons between satellite-retrieved
506 and surface-observed downwelling irradiances using the algorithm of *Li et al.* [1993] with and
507 without aerosol corrections [*Masuda et al.,* 1995] under clear-sky conditions. The retrievals
508 without the correction for the aerosol effect are larger than observed values by 46 Wm^{-2}. After
509 the correction, the bias is reduced to 8 Wm^{-2}. To implement the correction, one requires
510 aerosol optical properties, especially the AOD and SSA. A lack of SSA on a global scale may
511 induce considerable errors in the retrievals of the surface solar radiation budget over heavy
512 aerosol-loading regions, as is shown here and also in *Hayasaka et al. [2006]*, thus undermining

513 the estimation of the global radiation budget

514 Figure 11 shows a comparison of ARE at the TOA and at the surface. Note that the
515 surface ARE values are not identical to those shown in Fig. 8, which were derived from
516 measurements taken throughout a day, while those in Fig. 10 are instantaneous values
517 corresponding to satellite overpass times. Given the small number of data points, linear
518 regressions were performed for the clear-clean and clear-hazy data at the TOA and at the surface.
519 These functions were used to represent the actual data to overcome the small data sampling
520 issue. Four days falling on the equinoxes/solstices were chosen to represent the four seasons:
521 March 22, June 21, September 23 and December 22. It follows from Fig. 11 that the surface
522 ARE is more than 10 times that at the TOA. Their differences, often referred to as the
523 atmospheric aerosol effect, represent solar energy absorbed by aerosols in the boundary layer.
524 Such strong heating is bound to have a significant influence on atmospheric stability and thus on
525 atmospheric circulation and even cloud development. These aerosol-induced changes will be
526 studied and presented at a later date.

527

528 **6. Summary**

529

530 As the most populated and fastest developing country in the world, China is a region of
531 heavy aerosol loading with diverse physical, chemical, optical aerosol properties whose climatic
532 influence could be substantial, but remains largely uncertain. Improving the estimate of the
533 global aerosol effect on climate requires a good knowledge and understanding of aerosols in this
534 and many other major source regions. Unfortunately, many of the major aerosol emission
535 regions are severely under-sampled. To tackle the problem, an extensive observational program

536 was established in China as a joint scientific endeavor by American and Chinese scientists. One
537 major observation component is the establishment and operation of baseline stations that are
538 fully equipped in conformity with the international BSRN and AERONET networks. The first of
539 a series of planned baseline stations was set up in Xianghe, 70 km southeast of Beijing, in
540 September 2004. The site has provided quality-controlled continual observations of aerosol,
541 cloud and radiation quantities since its establishment. This paper presents some preliminary
542 results based on data collected for an entire year.

543 The most prominent finding is the high aerosol loading and dramatic changes in AOD
544 from day to day. The annual average AOD is 0.82 with maximum values exceeding 4. The AOD
545 generally increases steadily from a very low background value (less than 0.2) to very large
546 values in a few days (5-10 days) then drops sharply to a very low value in less than one day. The
547 sudden drops were usually caused by changes in airmass due to the passage of cold fronts. The
548 episodic increase of AOD was usually caused by the buildup of anthropogenic pollutants, as
549 indicated by the consistent episodes seen in simultaneous measurements of precursor gases such
550 as SO_2 and CO and NOy available during the IOP in March 2005. The retrieval of the single
551 scattering albedo from a Cimel sunphotometer showed a similar day-to-day fluctuation with a
552 mean value around 0.9. There is a weak seasonal trend with large and small values occurring
553 during the summer and late fall, respectively. The single scattering albedo increases with the
554 AOD, presumably due to an increasing proportion of sulfate aerosols.

555 The heavy aerosol loading poses a major challenge in identifying clear, hazy scenes from
556 cloudy scenes. Resorting to both automatic methods and manual inspection of the time series of
557 various radiative quantities and total sky image animations, we successfully classified all the
558 measurements into clear-clean (AOD<0.2), clear-hazy (AOD>0.2) and cloudy conditions. From

559 the classified data, aerosol and radiative effects were computed at the surface and at the TOA
560 using both ground-based and space-borne measurements. The aerosol radiative effect at the
561 surface is very large, with an annual mean of 25 Wm^{-2}, accounting for about half of the total
562 radiative effects by both clouds and aerosols (54 Wm^{-2}). However, the aerosol radiative effect at
563 the TOA is extremely small, about one tenth of the aerosol effect at the surface. This implies
564 that the majority of solar energy traveling toward the surface remained in the atmosphere in the
565 form of radiative heating. Such a strong adiabatic heating could have substantial influences on
566 atmospheric dynamics and cloud development and will be studied separately.
567
568 *Acknowledgements*: The EAST-AIRE project was supported by the NASA Radiation Science
569 Program (NNG04GE79G), the National Science Foundation of China (40250120071), and the
570 Chinese Academy of Sciences.
571

571
572 **References**
573
574

575 Bellouin, B., O. Boucher, J. Haywood, and M.S. Reddy (2005), Global estimates of aerosol direct
576 radiative forcing from satellite measurements, *Nature*, 438, 1138-1140, doi:10.1038/nature04348.
577 Bellouin, N., O. Boucher, D. Tanre, and O. Dubovik, 2003, Aerosol absorption over the clear-
578 sky oceans deduced from POLDER-1 and AERONET observations, *Geophy. Res. Lett.*,
579 30, doi:10.1029/2003GL017121.
580 Charlson, R. J., S.E. Schwartz, J. H. Hales, R.D. Cess, J.A. Coakley, Jr., J.E. Hansen, and D.J. Hofmann,
581 (1992): Climate forcing by anthropogenic aerosols, *Science*, 255, 423-430.
582 Chou, M.-D., Chan, P.-K., and Wang, M. (2002), Aerosol radiative forcing derived from SeaWiFS-
583 retrieved aerosol optical properties, *J. Atmos. Sci.*, 59, 748-757.
584 Chung, C. E., V. Ramanathan, D. Kim, and I. A. Podgorny (2005), Global anthropogenic aerosol direct
585 forcing derived from satellite and ground-based observations, *J. Geophy. Res.*, 110, D24207, doi:
586 10.1029/2005JD006356.
587 Conant, W.C., V. Ramanathan, and F.P.J. Valero, 1997: An examination of the clear-sky solar
588 absorption over the central equatorial Pacific: Observations versus models. *J. Clim.*, **10**,
589 1874-1884.
590 Dubovik, O., B. N. Holben, T. F. Eck, A. Smirnov, Y. J. Kaufman, M. D. King, D. Tanre, and I.
591 Slutsker (2002)**,** Variability of absorption and optical properties of key aerosol types
592 observed in worldwide locations, *J. Atmos. Sci.*, *59*, 590–608.
593 Eck, T., et al. (2005), Column aerosol optical properties at AERONET sites in central eastern
594 Asia and aerosol transport to the tropical mid-Pacific, *J. Geophy. Res.*, 110, D06202, doi:
595 10.1029/2004JD005274.

596 Eck, T.F., B.N. Holben, J.S. Reid, O. Dubovik, A. Smirnov, N.T. O'Neill, I. Slutsker, and S.
597 Kinne, Wavelength dependence of the optical depth of biomass burning, urban, and
598 desert dust aerosols, J. Geophys. Res., 104, 31,333 -31,349 , 1999.
599 Hansen, J., Sato, M., and Ruedy, R (1997).: Radiative forcing and climate response, J. Geophys. Res.,
600 102, 6831-6864.
601 Hayasak, T., K. Kawamoto, G. Shi, A. Ohmura (2006), Importance of aerosols in satellite-derived
602 estimates of surface shortwave irradiance over China, *Geophy. Res. Lett.*, 33,
603 10.1029/2005GL025093.
604 Holben, B.N., T.F., Eck, I. Slutsker, et al. (1998): AERONET - A federated instrument network and data
605 archive for aerosol characterization, *Remote Sens. Environ.*, 66, 1-16.
606 Huebert, B. J., T. Bates, P. B. Russell, G. Shi, Y. J. Kim, K. Kawamura, G. Carmichael, and T.
607 Nakajima (2003), An overview of ACE-Asia: Strategies for quantifying the relationships
608 between Asian aerosols and their climatic impacts, *J. Geophys. Res.*, *108*(D23), 8633,
609 doi:10.1029/2003JD003550.
610 Huebert et al. (2006), in preparation.
611 Intergovernmental Panel on Climate Chang (IPCC) (2001), *Climate Change 2001: The Scientific*
612 *Basis*, edited by J. T. Houghton et al., 881 pp., Cambridge Univ. Press, New York.
613 Jeong, M.J., Z. Li, E. Andrews, and S.-C. Tsay, 2006, Effect of Aerosol Humidification on the
614 Column Aerosol Optical Thickness over the ARM Southern Great Plains Site, *J. Geophy.*
615 *Res.*, submitted.
616 Kaufman, Y.J., D. Tanré, O. Dubovik, A. Karnieli, L.A. Remer (2001): Absorption of sunlight by dust as
617 inferred from satellite and ground-based measurements, *Geophys. Res., Lett.*, 28, 1479-1482.
618 Kaufman, Y. J., D. Tanré, and O. Boucher (2002): A satellite view of aerosols in the climate system,
619 Nature, 419, doi:10.1038/nature01091.

620 Kaufman, Y.J., J.V., Martins, L.A. Remer, M.R. Schoeberl, and M.A. Yamasoe (2002): Satellite retrieval
621 of aerosol absorption over the oceans using sunglint, *Geophys. Res. Lett.*, 29 (19), 1928,
622 doi:10.1029/2002GL015403.
623 Kaufman Y.J., G. P. Gobbi, I. Koren, (2005), Aerosol climatology using a tunable spectral
624 variability cloud screening of AERONET data, *Geophy. Res. Lett.*, accepted.
625 Kim, D., B. Sohn, T. Nakajima, T. Takamura, T. Takemura, B. Choi, and S. Yoon (2004),
626 Aerosol optical properties over east Asia determined from ground-based sky radiation
627 measurements, *J. Geophys. Res.*, *109*, D02209, doi:10.1029/2003JD003387.
628 Kim, D.-H., B. J. Sohn, T. Nakajima, and T. Takamura (2005), Aerosol radiative forcing over
629 east Asia determined from ground-based solar radiation measurements, *J. Geophys. Res.*,
630 *110*, D10S22, doi:10.1029/2004JD004678.
631 King, M. D., Y.J. Kaufman, D. Tanré, and T. Nakajima (1999), Remote sensing of tropospheric aerosols:
632 Past, present, and future, *Bull. Am. Meteorol. Soc.*, 80, 2229-2259.
633 Li, Z., H.G. Leighton, K. Masuda, and T. Takashima (1993), Estimation of SW flux absorbed at
634 the surface from TOA reflected flux, *J. Climate*, **6,** 317-330.
635 Li, Z., 1998, Influence of absorbing aerosols on the inference of solar surface radiation budget
636 and cloud absorption, *J. Climate,* **11,** 5-17.
637 Li, Z., 2004, Aerosol and climate: A perspective from East Asia, in "*Observation, Theory, and*
638 *Modeling of the Atmospheric Variability*", p501-525, World Scientific Pub. Co..
639 Li, Z., and L. Garand, 1994: Estimation of surface albedo from space: A parameterization for
640 global application, *J. Geophy. Res*., **99,** 8335-8350.
641 Li, Z., and L. Kou, 1998, Atmospheric direct radiative forcing by smoke aerosols determined
642 from satellite and surface measurements, *Tellus (B)*, **50**, 543-554.

643 Li, Z., and A. Trishchenko (2001), Quantifying the uncertainties in determining SW cloud
644 radiative forcing and cloud absorption due to variability in atmospheric condition, *J.*
645 *Atmos. Sci.*, 58, 376-389.
646 Li, C., L.T. Marufu, R.R. Dickerson, Z. Li, T. Wen, Y. Wang, P. Wang, H. Chen, J.W. Stehr
647 (2006), In-situ measurements of trace gases and aerosol optical properties at a rural site in
648 Northern China during EAST-AIRE IOP 2005, J. Geophy. Res. (to be submitted as a
649 companion paper).
650 Liao, H., J. H. Seinfeld, P. J. Adams, and L. J. Mickley (2004), Global radiative forcing of
651 coupled tropospheric ozone and aerosols in a unified general circulation model, *J.*
652 *Geophys. Res*., **109**, D16207, doi:10.1029/2003JD004456.
653 Loeb, N. G. and N. Manalo-Smith (2005): Top-of-atmosphere direct radiative effect of aerosols
654 over global oceans from merged CERES and MODIS observations, *J. Clim.*, **18**, 3506-
655 3526.
656 Loeb, N. G., S. Kato, K. Loukachine, and N. manalo-Smith (2005): Angular distribution models
657 for top-of-atmosphere radiative flux estimation from the Clouds and the Earth's Radiant
658 Energy System instrument on the Terra satellite. Part I: Methodology, *J. Atmos. Ocean.*
659 *Tech*., **22**, 338-351.
660 Long, C.N. and T.P. Ackerman, 2000: Identification of clear skies from broadband pyranometers
661 measurements and calculation of downwelling shortwave cloud effects. *J. Geophys. Res.*,
662 **105**, 15609-15626.
663 Masuda, K., H.G. Leighton, and Z. Li (1995), A new parameterization for the determination of
664 solar flux absorbed at the surface from satellite measurements, *J. Climate*, *8***,** 1615-1629.

665 Nakajima, T., et al. (2003), Significance of direct and indirect radiative forcings of aerosols in
666 the East China Sea region, *J. Geophys. Res.*, *108*(D23), 8658,
667 doi:10.1029/2002JD003261.
668 Nakajima, T.and M. Tanaka (1988), Algorithms for radiative intensity calculations in moderately
669 thick atmospheres using a truncation approximation, *J. Quant. Spectrosc. Radia*t.
670 *Transfer, 40*, 51-69.
671 Ohmura, A., et al. (1998), Baseline Surface Radiation Network (BSRN)/WCRP), a new precision
672 radiometry for climate research, *Bull. Am. Meteorol. Soc.*, *79*, 2115–2136.
673 Ramanathan, V., P. J. Crutzen, J. T. Kiehl, and D. Rosenfeld (2001a), Aerosol, climate, and
674 hydrological cycle, *Science*, *294*, 2119–2124.
675 Ramanathan, V., et al. (2001b), Indian Ocean Experiment: An integrated analysis of the climate
676 forcing and effects of the great Indo-Asian haze, *J. Geophys. Res.*, *106*, 28,371–28,398.
677 Remer, L. A., and Kaufman, Y. J., (2005), Aerosol effect on the distribution of solar radiation over the
678 global oceans derived from five years of MODIS retrievals, *Atmos. Chem. Phys. Discuss.*, 5,
679 5007-5038. SRef-ID: 1680-7375/acpd/2005-5-5007.
680 Rosenfeld, D., and Lensky, I. M. (1998): Satellite-based insights into precipitation formation processes in
681 continental and maritime convective clouds, Bull. Am. Met. Soc., 79, 2457-2476.
682 Smirnov A., B.N. Holben, T.F. Eck, O. Dubovik, and I. Slutsker (2000), Cloud screening and quality
683 control algorithms for the AERONET database, *Rem. Sens. Env.*, *73*, 337-349, 2000.
684 Takemura, T., T. Nozawa, S. Emori, T.Y. Nakajima, and T. Nakajima (2005): Simulation of climate
685 response to aerosol direct and indirect effects with aerosol transport-radiation model, *J. Geophys.*
686 *Res.*, 110, D02202, doi:10.1029/2004JD005029.
687 Satheesh, S. K., and V. Ramanathan (2000), Large differences in the tropical aerosol forcing at
688 the top of the atmosphere and Earth's surface, *Nature*, *405*, 60–63.

689 Schafer, J.S., T. F. Eck, B. N. Holben, P. Artaxo, M. A. Yamasoe, and A. S. Procopio, Observed
690 reductions of total solar irradiance by biomass-burning aerosols in the Brazilian Amazon and
691 Zambian Savanna, Geophys. Res. Lett., 29, 1823, doi:10.1029/2001GL014309, 2002.
692 Wielicki, B.A., et al., 1996, Clouds and the Earth's Radiant Energy System (CERES): An Earth
693 Observation System experiment, *Bull. Amer. Meteor. Soc.*, 77, 853-868.
694 Xin, J., Y. Wang, Z. Li, P. Wang, W.-M. Hao (2006), Aerosol optical depths observed across
695 China using hand-held sunphotometers, *J. Geophy. Res.*, submitted.
696 Yu, H., R.E. Dickinson, M. Chin, Y.J. Kaufman, M. Zhou, L. Zhou, Y. Tian, O. Dubovik, and
697 B.N. Holben, 2004, Direct radiative effect of aerosols as determined from a combination
698 of MODIS retrievals and GOCART simulations, *J. Geophy. Res.*, 109,
699 doi:10.1029/2003JD03206.
700 Zhang, Y., W.B. Rossow, A.A. Lacis, V. Oinas and M.I. Mishchenko (2004), Calculation of
701 radiative fluxes from the surface to top-of-atmosphere based on ISCCP and other global
702 datasets: Refinements of the radiative transfer model and the input data, *J. Geophy. Res., 109*, D19105.
704

Figure Captions

Figure 1. Daily mean aerosol optical depths measured by a Cimel sunphotometer from October 2004 to September 2005 at the Xianghe site. The dashed curve shows the 10-day running averages of the AOD.

Figure 2. Relationship between the Angstrom exponent and the aerosol optical depth for Cimel data from September 2004 to September 2005.

Figure 3. The relationships between the aerosol optical depth and relative humidity for data from December 21, 2004 to July 11, 2005 (left panel) and for June 2005 only (right panel).

Figure 4. The day-to-day variation of daily mean aerosol optical depths in October 2004 (upper panel) and corresponding surface direct solar irradiances (bottom panel).

Figure 5. Daily mean single scattering albedos (corresponding to AOD at 440 nm > 0.4) retrieved from the Cimel sky radiances at 441, 673, 873 and 1022 nm. Data are from September 2004 to September 2005. Overall average at each wavelength in parentheses.

Figure 6. The variations of single scattering albedo with the aerosol optical depth (upper panel) and the Angstrom exponent (lower panel).

Figure 7. The variation of surface downwelling irradiances with the cosine of the solar zenith angle for cloud-free (upper panel), cloudy (middle panel) and all data (bottom panel) observed in March 2005.

Figure 8. Monthly means of the aerosol radiative effect, cloud radiative effect and total effects at the surface.

Figure 9. Solar irradiance reflected at the top of the atmosphere (upper panel; from the CERES SSF product) and incoming on the ground (lower panel; measured) for clear-clean (AOD<0.2) and clear-hazy conditions (AOD>0.2). CHANGES: Use B&W symbles. Change the Y labels to “Reflected Irradiance” and “Downwelling Irradiance”

Figure 10. Comparison between satellite retrieved and surface observed solar irradiance without and with aerosol corrections using the algorithms of Li et al. (1993) and Masuda et al. (1995).

Figure 11. Comparison between the aerosol radiative effects at the top of the atmosphere and at the surface for all matched ground and satellite (CERES) observations.

748

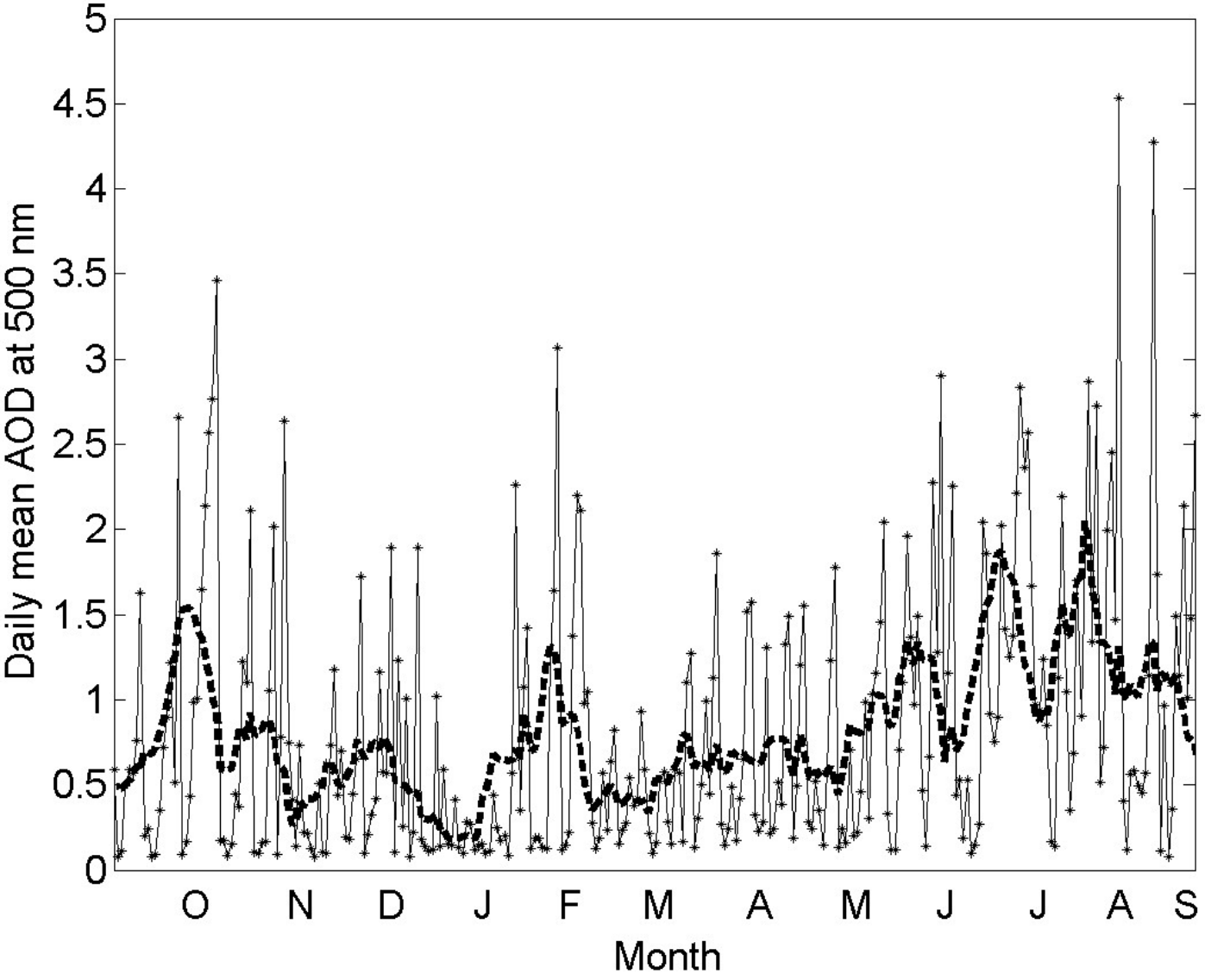

749

750 Figure 1. Daily mean aerosol optical depths measured by a Cimel sunphotometer from October
751 2004 to September 2005 at the Xianghe site. The dashed curve shows the 10-day
752 running averages of the AOD.
753
754

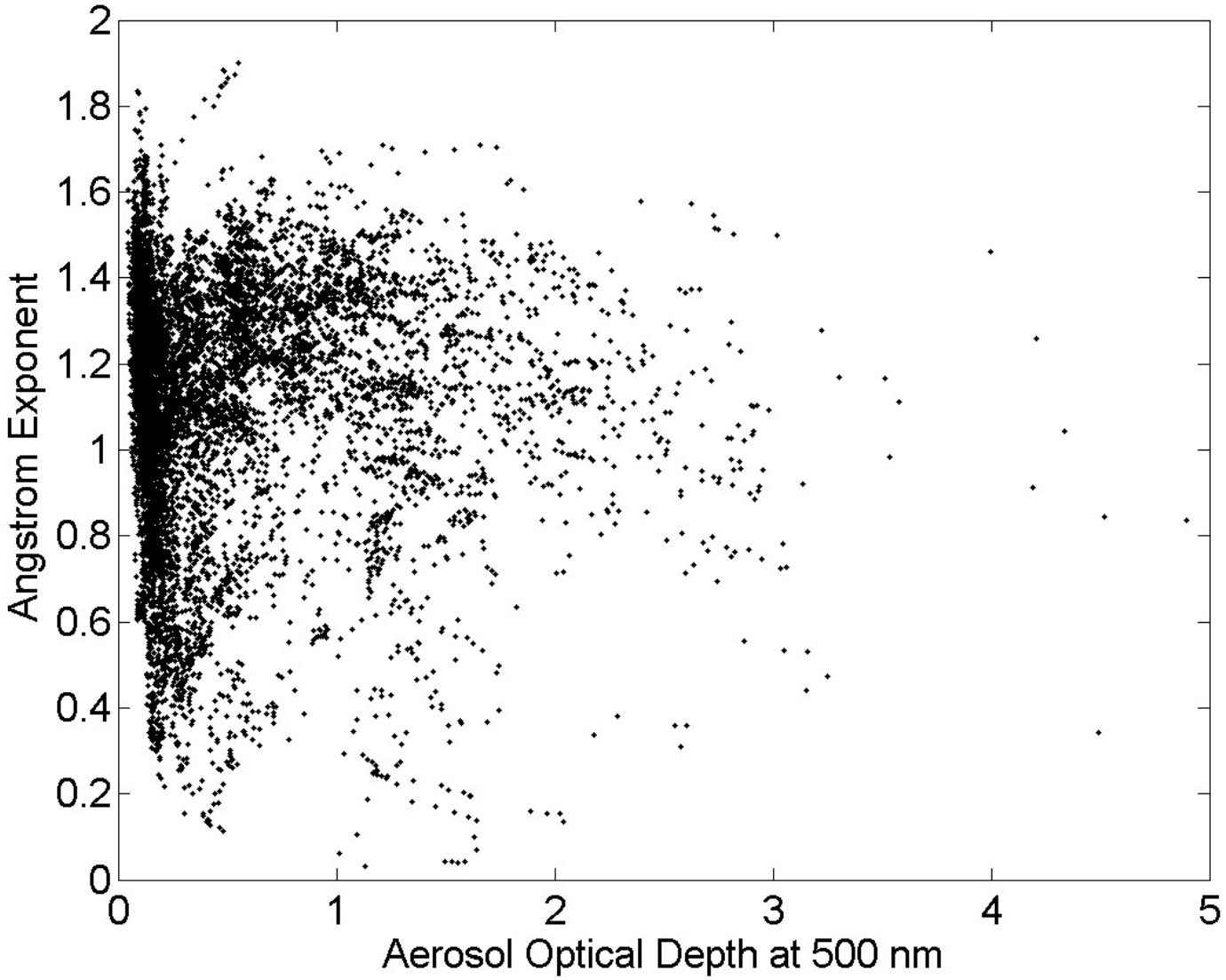

754 Figure 2. Relationship between the Angstrom exponent and the aerosol optical depth for
755 Cimel data from September 2004 to September 2005.
756
757
758
759

759

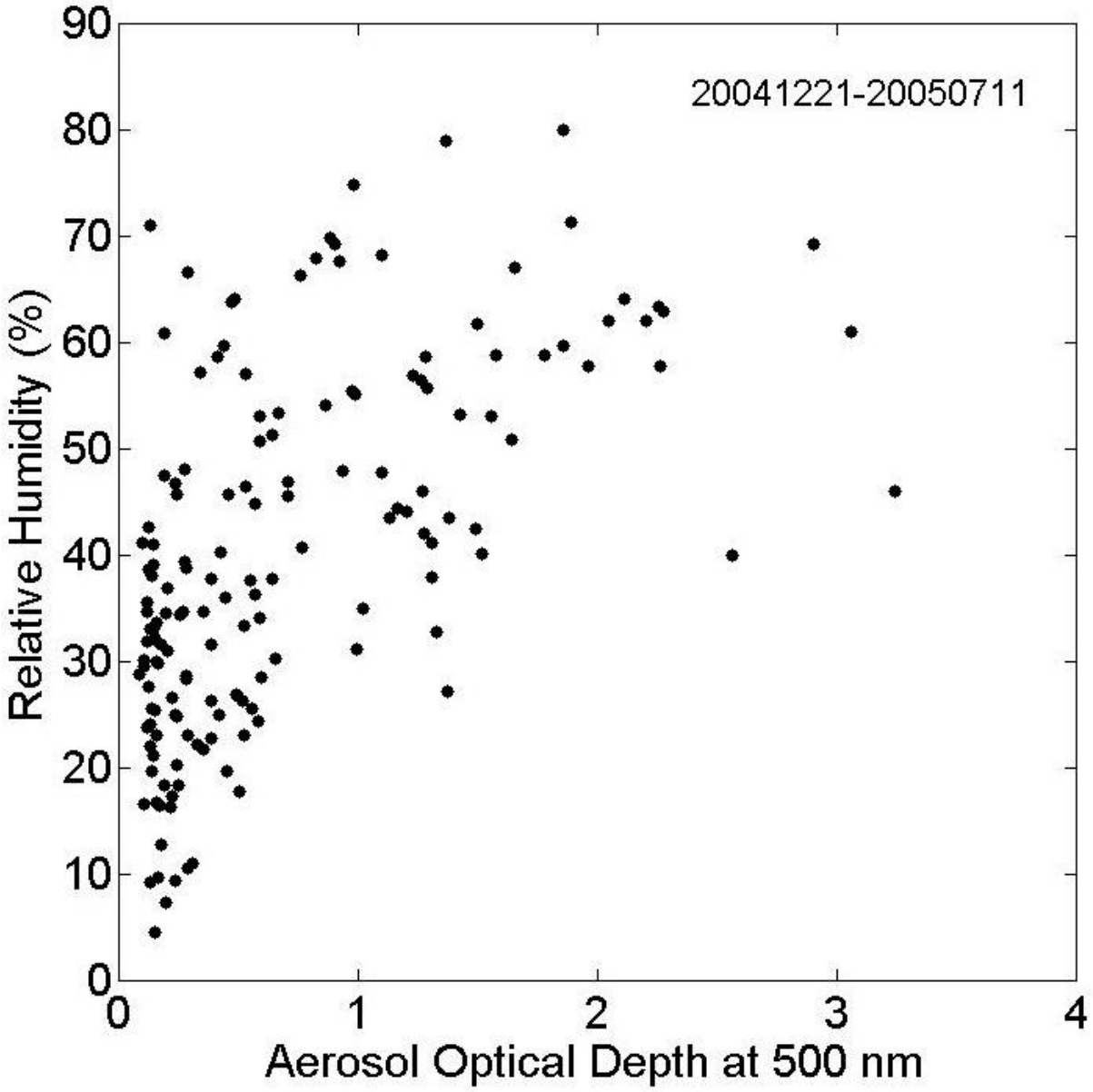

760

761 Figure 3. The relationships between the aerosol optical depth and relative humidity for data from
762 December 21, 2004 to July 11, 2005 (left panel) and for June 2005 only (right panel).

763

764

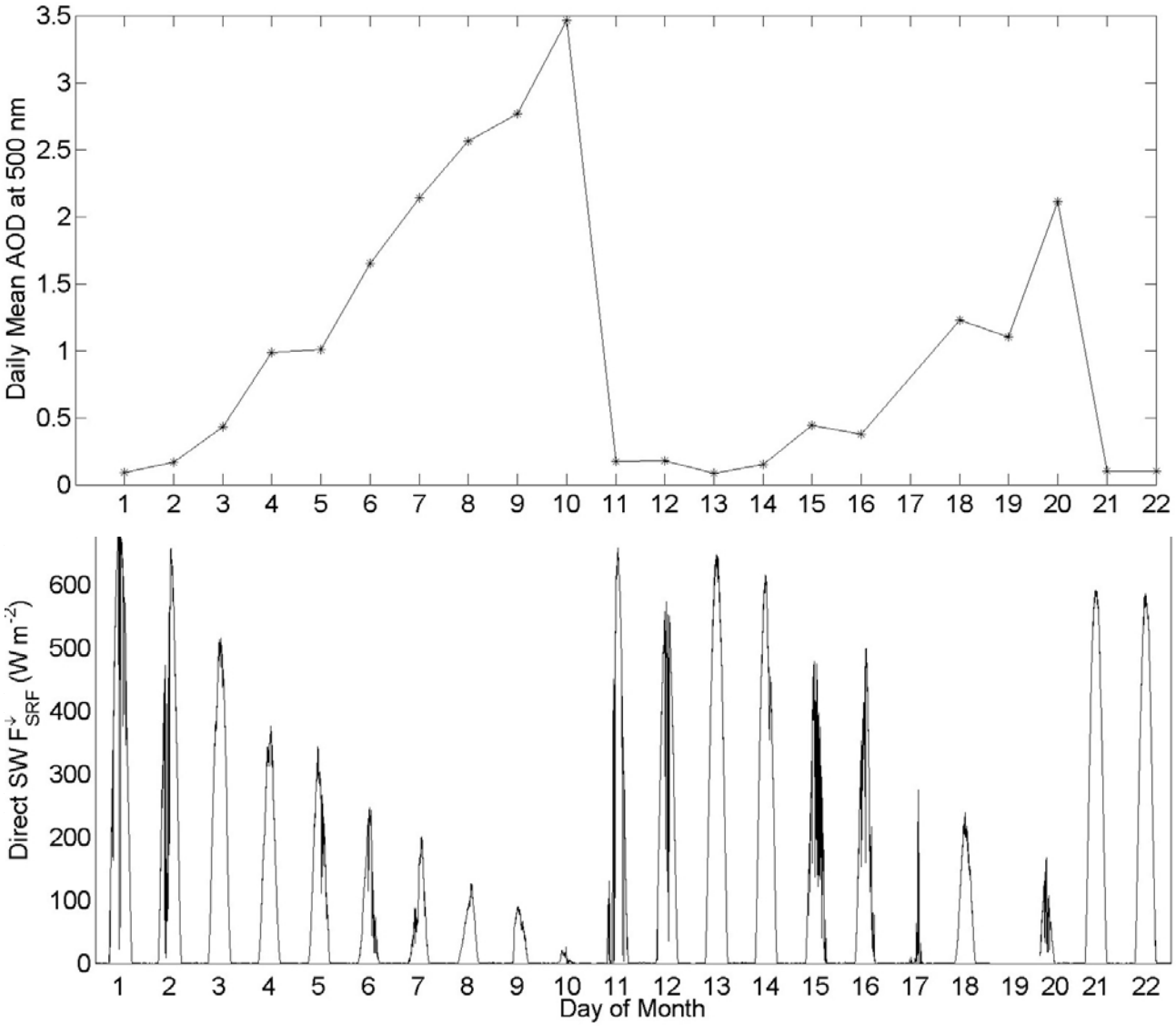

Figure 4. The day-to-day variation of daily mean aerosol optical depths in October 2004 (upper panel) and corresponding surface direct solar irradiances (bottom panel).

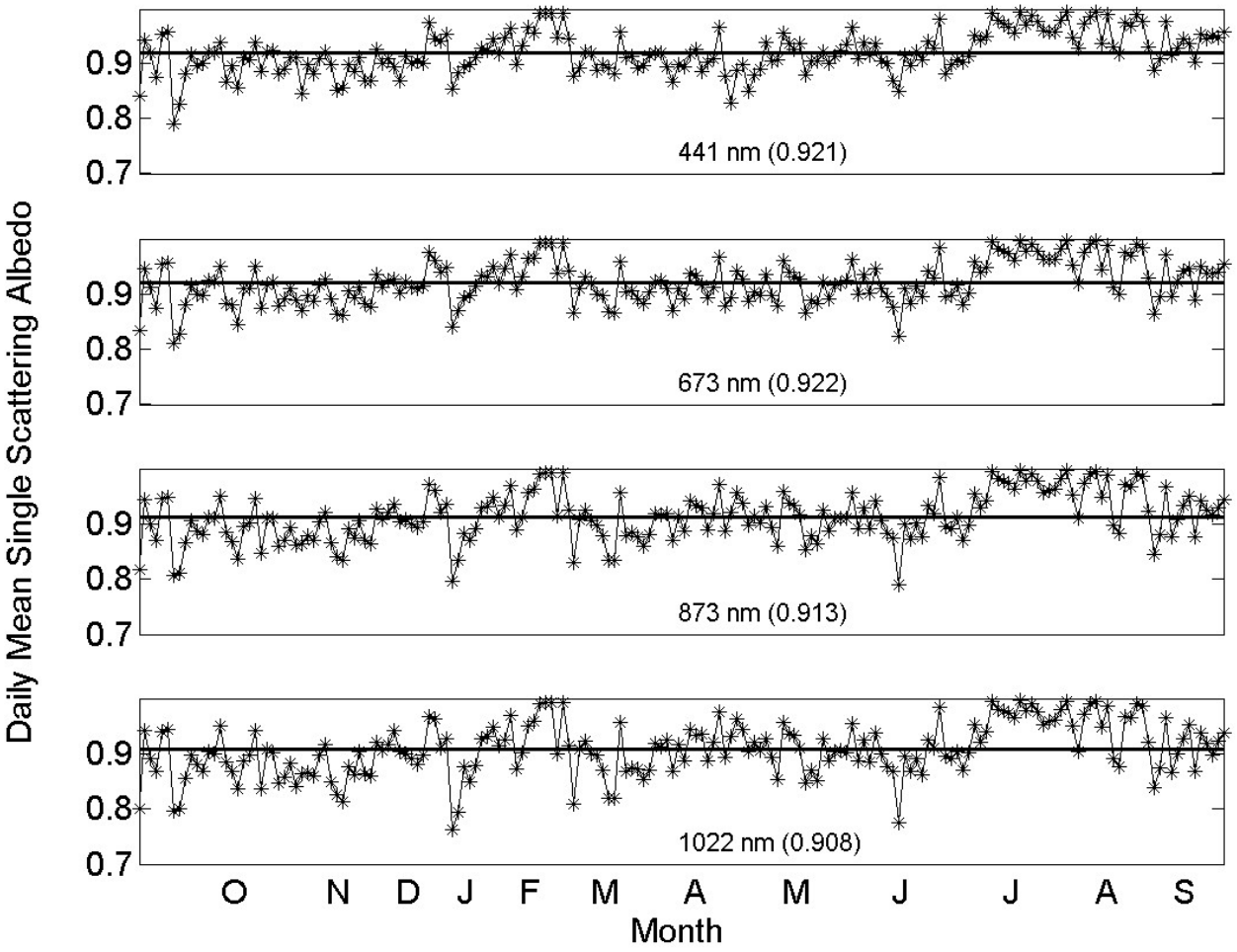

Figure 5. Daily mean single scattering albedos (corresponding to AOD at 440 nm > 0.4) retrieved from the Cimel sky radiances at 441, 673, 873 and 1022 nm. Data are from September 2004 to September 2005. Overall average at each wavelength in parentheses.

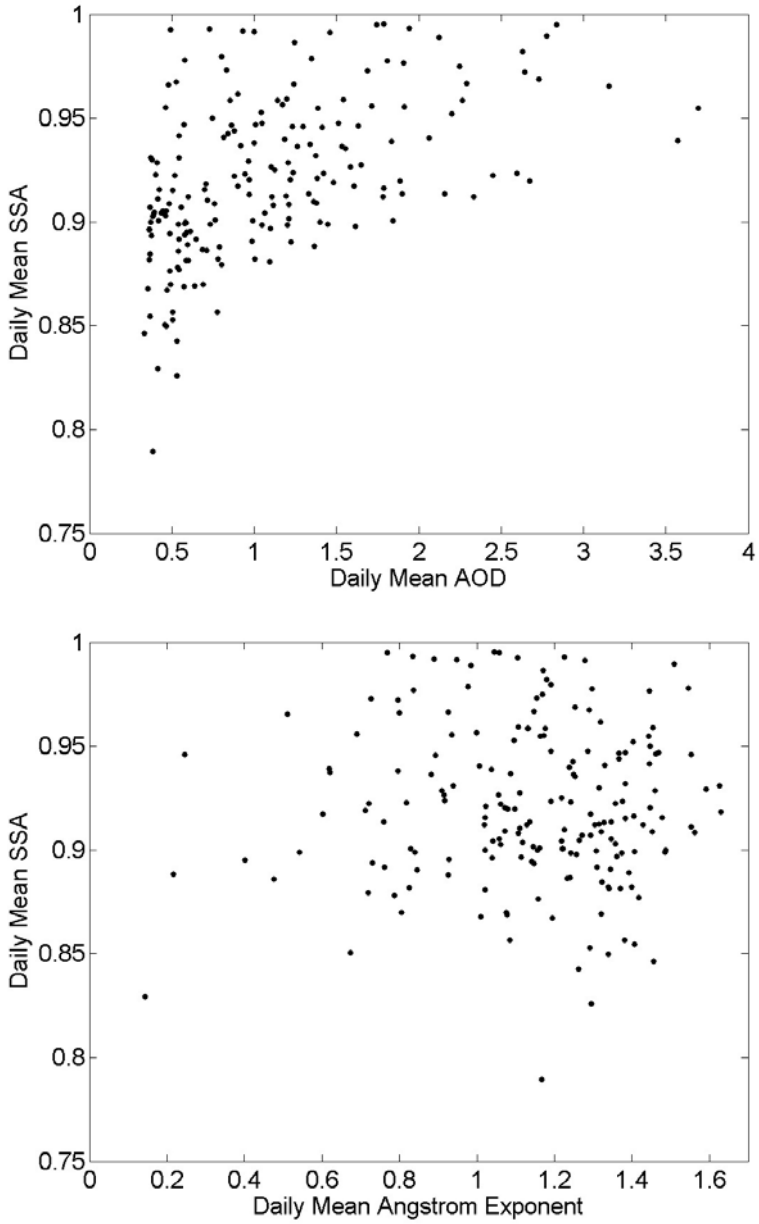

Figure 6. The variations of single scattering albedo with the aerosol optical depth (upper panel) and the Angstrom exponent (lower panel).

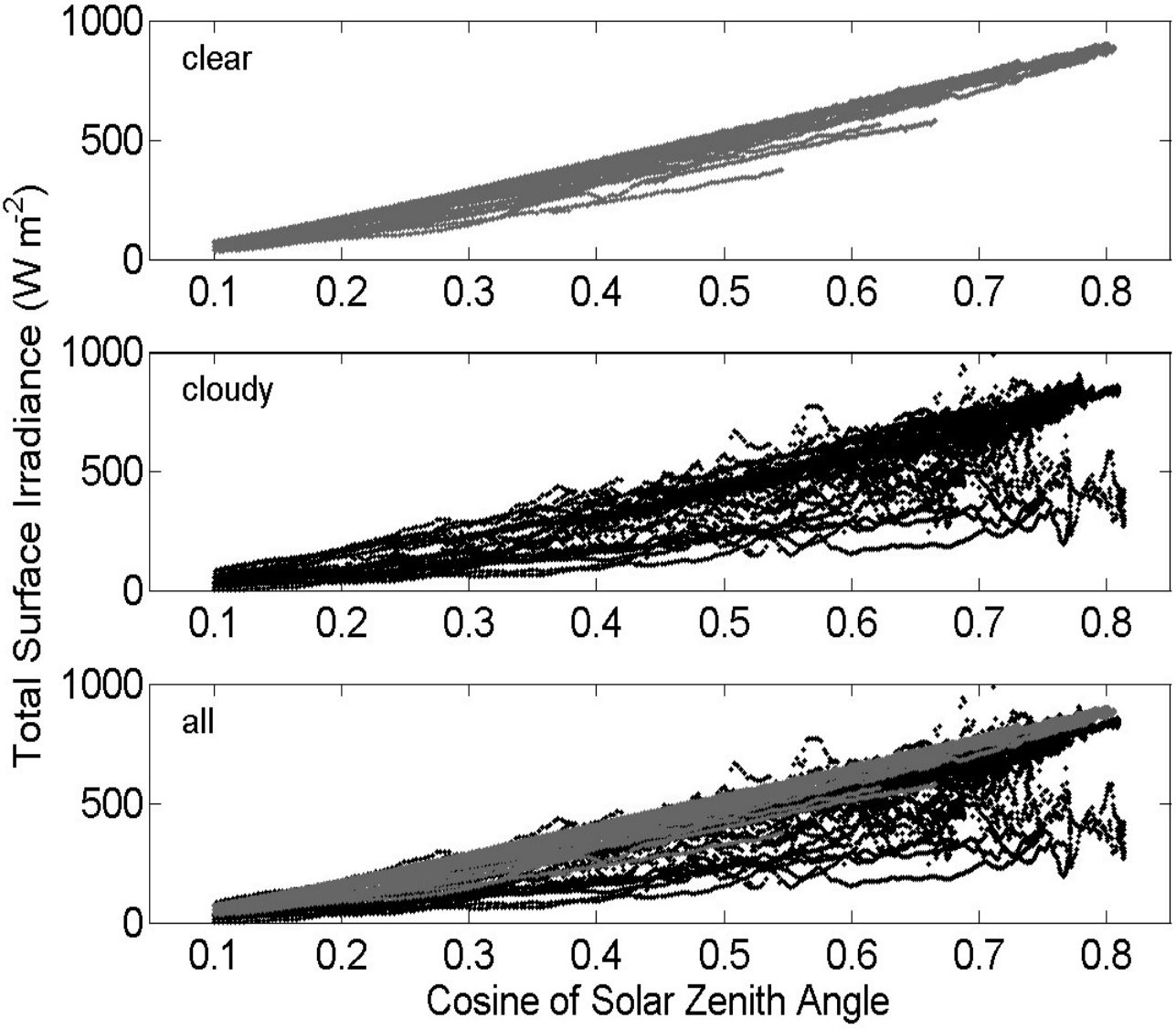

849
850 Figure 7. The variation of surface downwelling irradiances with the cosine of the solar zenith
851 angle for cloud-free (upper panel), cloudy (middle panel) and all data (bottom panel)
852 observed in March 2005.
853
854

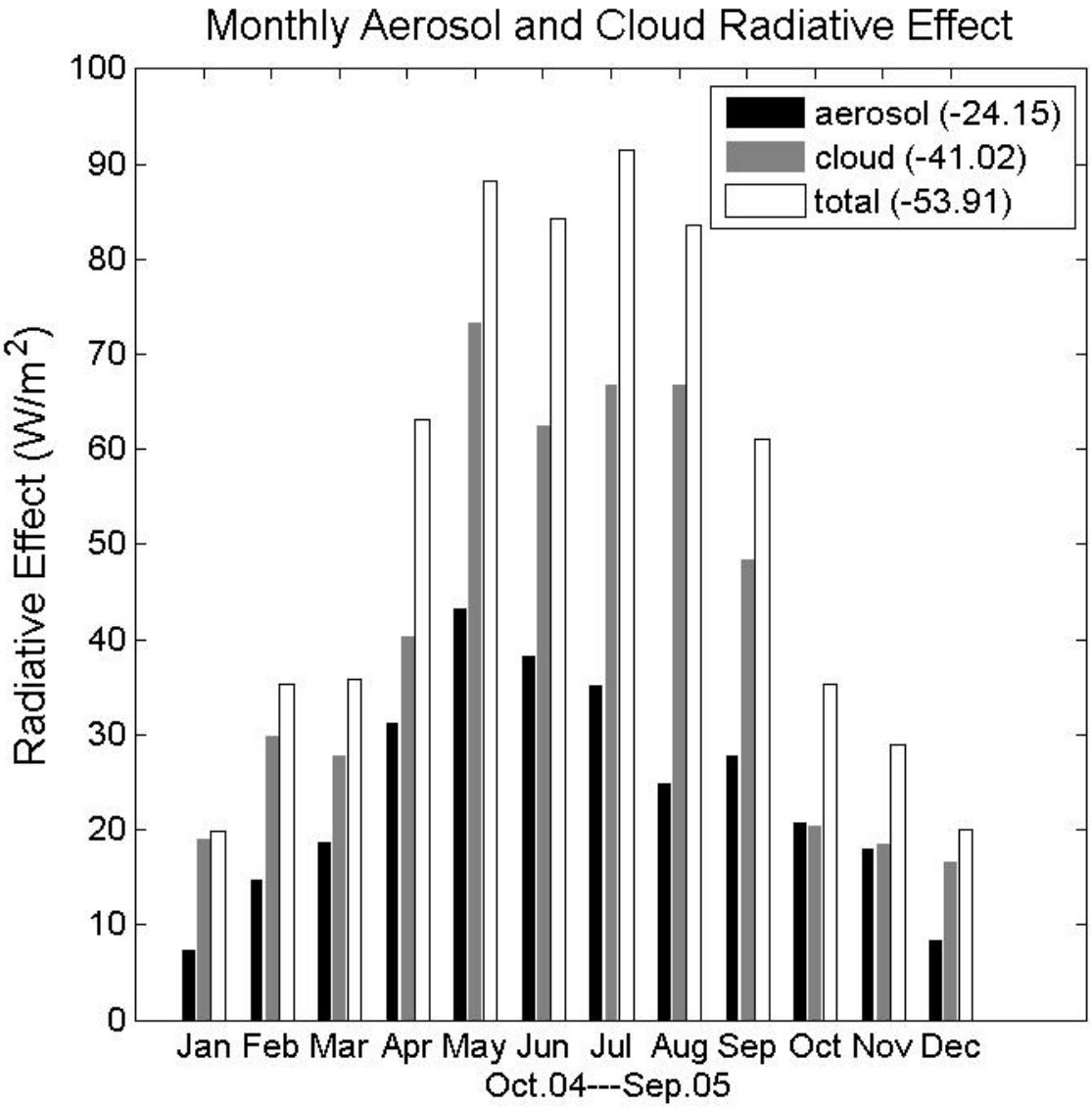

Figure 8. Monthly means of the aerosol radiative effect, cloud radiative effect and total effects at the surface.

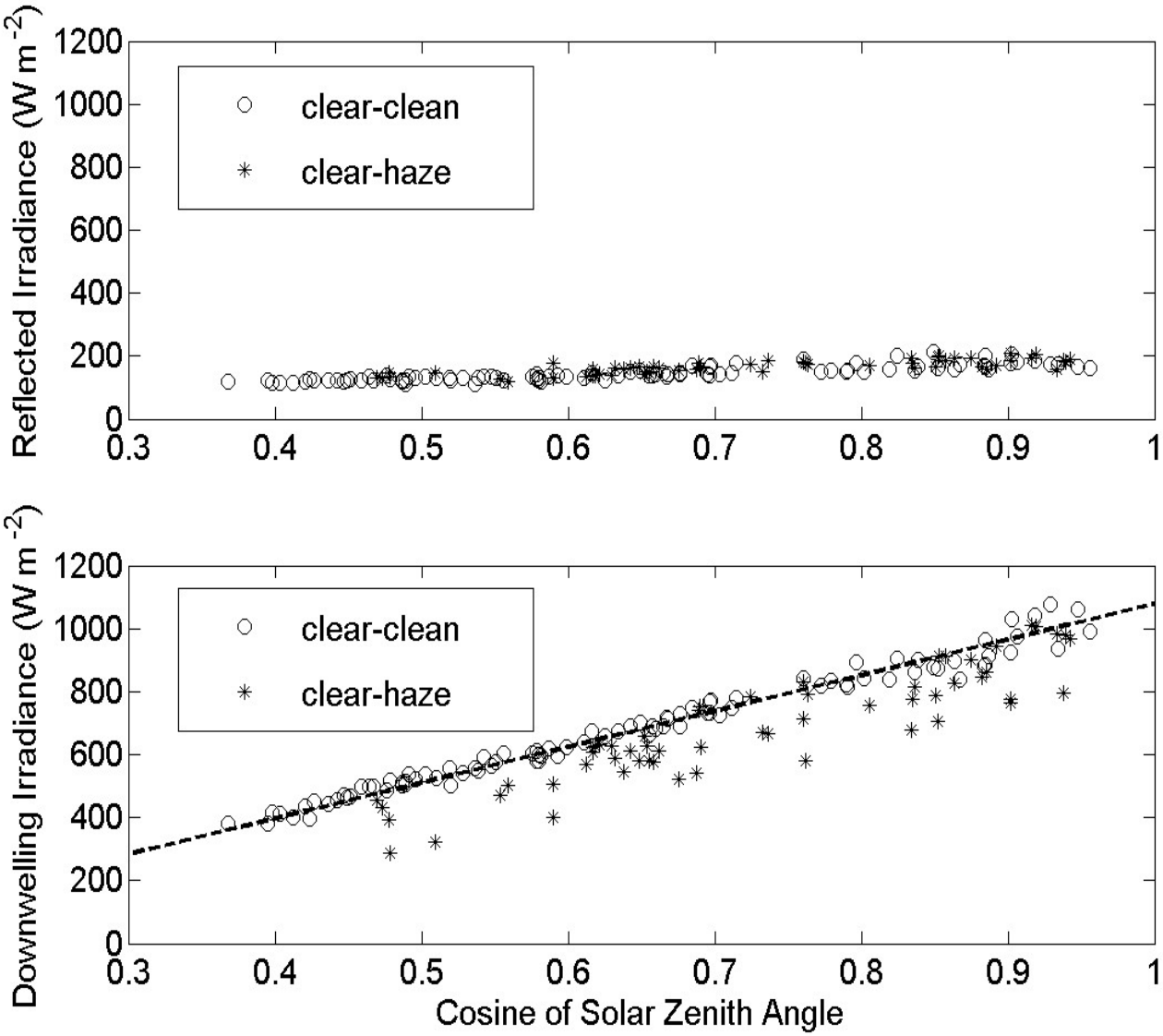

Figure 9. Solar irradiance reflected at the top of the atmosphere (upper panel; from the CERES SSF product) and incoming on the ground (lower panel; measured) for clear-clean (AOD<0.2) and clear-hazy conditions (AOD>0.2). CHANGES: Use B&W symbles. Change the Y labels to "Reflected Irradiance" and "Downwelling Irradiance"

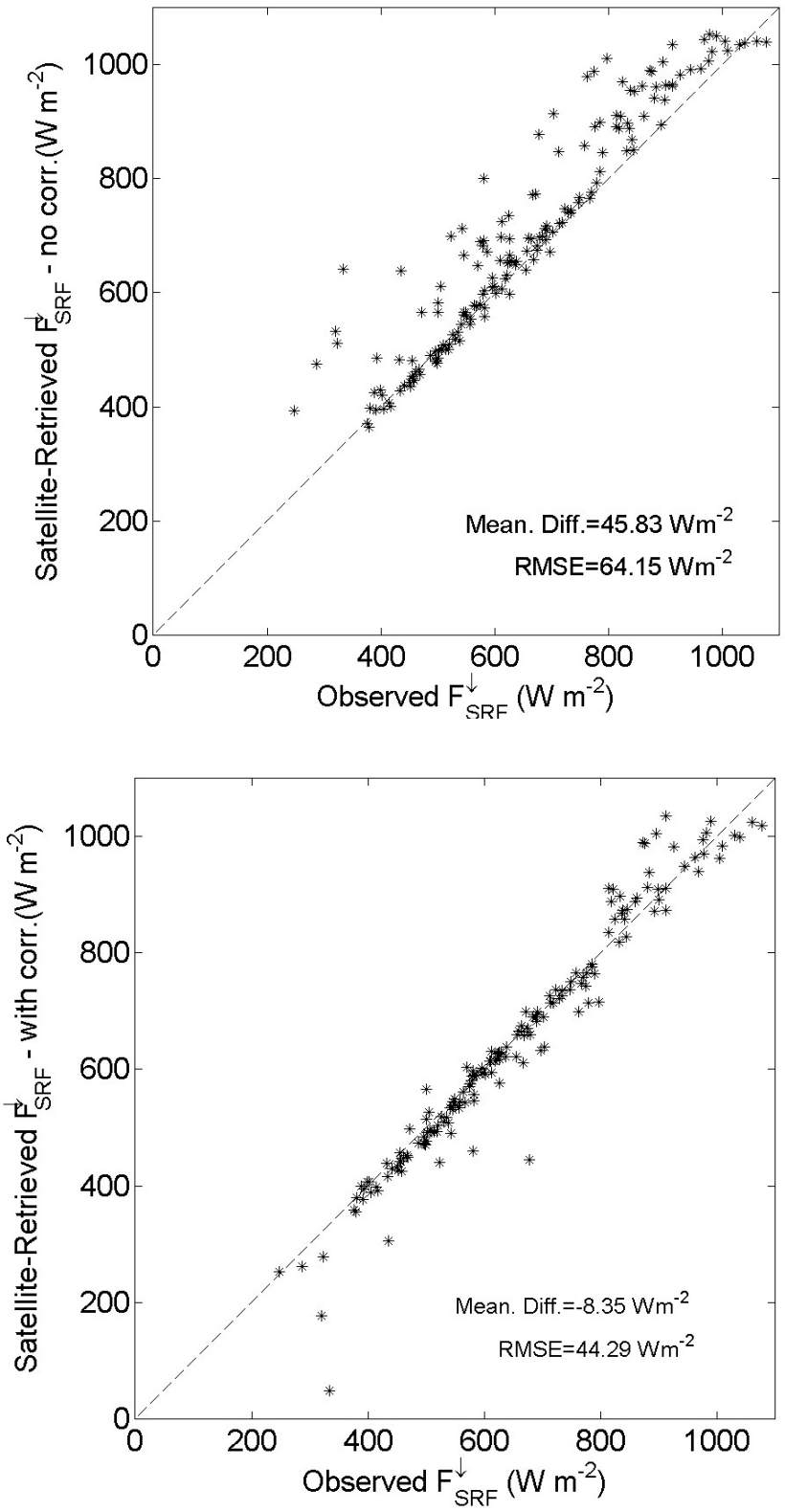

Figure 10. Comparison between satellite retrieved and surface observed solar irradiance without and with aerosol corrections using the algorithms of Li et al. (1993) and Masuda et al. (1995).

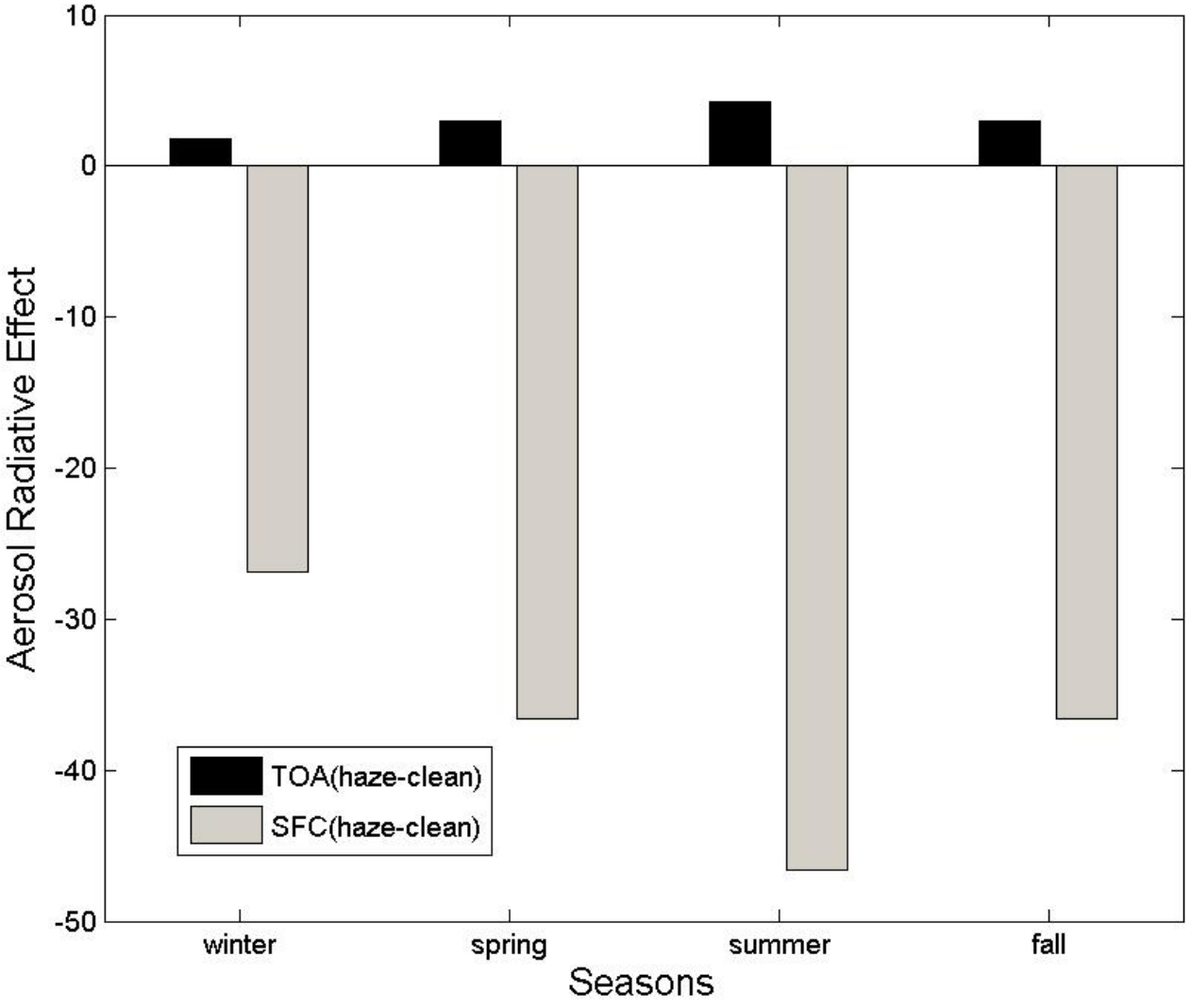

871 Figure 11. Comparison between the aerosol radiative effects at the top of the atmosphere and at
872 the surface for all matched ground and satellite (CERES) observations.
873